

# Rapid Flow Surveys via Rotating Rake System and Use in Powered Wind Tunnel Models

Michael Lieu\*, Alejandra Uranga†, Mark Drela‡ and Edward Greitzer§

*Massachusetts Institute of Technology, Cambridge, MA 02139, U.S.A.*

This paper describes a rotating rake system for rapid measurement of total and static pressure distributions in powered airframe models with complex geometries. The local actuation of the rake rotation mechanism allows access to regions of the flow not easily accessible to traditional traverse systems with wall-mounted leadscrew actuators. Local indexing of the rake pivot to the model precisely positions the rake in the presence of model vibration. The total and static rakes and mechanisms are built from commercially available hardware and materials.

The rotating rake system was employed to measure total and static pressures in the propulsive streamtubes of a boundary-layer ingesting powered aircraft model in the NASA Langley 14'×22' wind tunnel. The specific quantity of interest was the total pressure flux into and out of the propulsors, needed to quantify the power-saving benefits of the boundary layer ingestion system.

The paper discusses the benefits and drawbacks of the rotating rake system for the demonstrated wind tunnel experiment and for more general flow measurements.

## Nomenclature

$A_{\text{fan}}$	fan area (= 25.25 in <sup>2</sup> )	$\alpha$	model angle of attack
$A_{\text{jet}}$	jet area	$\beta$	model sideslip angle
$c_{\text{ref}}$	model reference chord (= 10.75 in)	$\theta_{\text{rad}}$	radial flow angle
$C_p$	static pressure coefficient	$\theta_{\text{swl}}$	swirl flow angle
$C_{p_o}$	total pressure coefficient	$\mu$	air viscosity
$C_{p_{\text{st}}}$	streamtube boundary threshold $C_{p_o}$	$\rho$	air density
$\tilde{C}_{PK}$	jet total pressure flux coefficient	$( )_{\infty}$	Free-stream (wind-tunnel) quantity
$C_X$	net stream-wise force coefficient	$\Delta( )$	perturbation quantity or uncertainty
$D_{\text{fan}}$	fan diameter (=5.67 in <sup>2</sup> )		
$\dot{m}_{\text{jet}}$	jet mass flow		
$\hat{n}$	unit normal vector		
$p$	static pressure		
$p_o$	total pressure		
$q$	dynamic pressure		
$Re$	Reynolds number ( = $\rho V_{\infty} c_{\text{ref}} / \mu$ )		
$S_{\text{ref}}$	model reference area (= 1686 in <sup>2</sup> )		
$U_{\text{tip}}$	fan tip speed		
$\vec{V}$	velocity vector		
$V$	speed		

\*Graduate Student, Dept. of Aeronautics and Astronautics, mlieu28@mit.edu, AIAA Student Member.

†Research Engineer, Dept. of Aeronautics and Astronautics, auranga@mit.edu, AIAA Member.

‡Terry J. Kohler Professor of Fluid Dynamics, Dept. of Aeronautics and Astronautics, AIAA Fellow.

§H.N. Slater Professor of Aeronautics and Astronautics, Dept. of Aeronautics and Astronautics, AIAA Honorary Fellow.

## I. Introduction

THERE is a common need to survey and characterize flow coming into or out of propulsors. Five-hole probe traverses are often used for detailed propulsor exit flow surveys, while mounted rakes are used to characterize the inlet flow. These forms of measurements have their own drawbacks; five-hole probe surveys can be time consuming while mounted rakes can only obtain pressure data in a specific area. For time-sensitive experiments that require full flow field surveys to visualize the flow or calculate integrated quantities, a rotating rake systems is a viable option.

Measurements from a rotating rake are relatively quicker to obtain. Rakes have the advantage of measuring entire radial profiles simultaneously, in contrast to a 2D actuated, five-hole probe traverse where one spatial point is measured at a time. Rotating rake systems are also better suited for applications that require direct pressure measurements, as opposed to methods like particle image velocimetry where pressures must be post-processed from velocity data.

Rotating rake systems are not uncommon. For example, Sutliff's<sup>1</sup> propulsor aero-acoustic experiment featured a rake on a rotating drum wheel mounted on the outside the circumference of the propulsor. Typical rotating rake systems use the rotating drum concept to survey the flow, but this setup can be cumbersome and expensive. The rotating drum works best for isolated propulsor experiments, but becomes too bulky for experiments that require flow surveys in locations where access is limited.

The rotating rake system described in this paper has specific applications to scaled, powered airframe experiments, but the concept could be extended to larger experiments. The system is compact which allows access to measurement planes not normally accessible with traditional setups, such as the planes upstream of the propulsor. This also forgoes the need to conduct isolated experiments that simulate incoming flow off the airframe since the surveys can be taken directly on the airframe model. The rotating rake system features an indexing capability which allows for spatial repeatability. This system is cost effective which is beneficial for academic level experiments since many of the components are commercially available.

The rotating rake system discussed in this paper was applied to the MIT N+3 airframe experiments. The NASA N+3 project challenged teams from academia and industry to re-imagine commercial aviation in the year 2035 assuming certain technology advancements. Many of the driving factors for the project involved reducing the impact commercial aviation has on the environment, specifically fuel burn, emissions, and noise. MIT, partnered with Aurora Flight Sciences and Pratt & Whitney presented the D8 configuration that featured a lifting body fuselage, pi-tail, unswept wings, and flush-aft mounted engines. The D8 aircraft would theoretically reduced fuel burn by 70% with a large percentage of this reduction from the concept of boundary layer ingesting engines.<sup>4</sup>

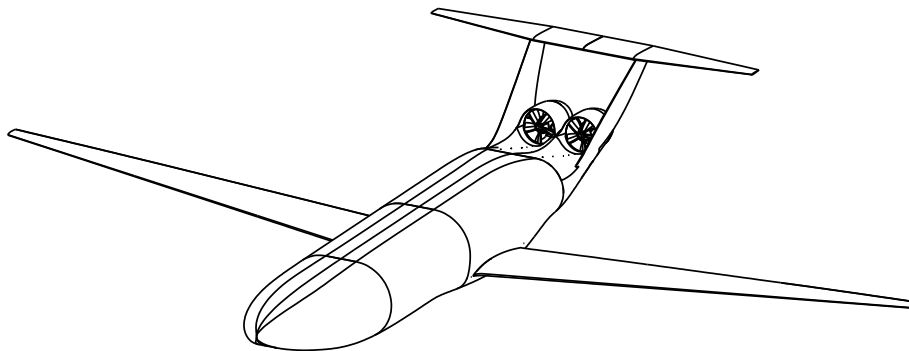


Figure 1: D8 aircraft model used in experiments.

Currently the N+3 project is geared towards experimental evaluation of boundary layer ingestion (BLI). These experiments features an assessment of a 1:11 scaled powered aircraft using commercial off-the-shelf electric ducted fan units in place of the engines shown in Figure 1. The model consists of 3D-printed aero shells mounted on a steel sub-structure, and features a common fuselage and wings with interchangeable tails. The main interest for the experimental assessment is the mechanical flow power<sup>3</sup> of the airframe which is related to the total pressure flux through the propulsor units. To measure the total pressure flux, direct measurements of total and static pressure were needed at planes upstream and downstream of the propulsors. The rotating rake system provided a practical way of measuring the flow field and providing the

total pressure flux on the model airframe.

## II. Pressure Rakes

### A. Rake Overview

In order to measure the total and static pressure fields of the propulsor inlet and exit, separate total and static rakes were manufactured for the rotating rake system. Although the total and static rakes do not provide flow direction information, this still allowed the measurement of the jet total pressure flux to an acceptable level of accuracy.

The design of the rakes were based on the size of the propulsor and any predicted flow features that needed resolution. Both rakes used in the experiments were made in-house using readily available materials and equipment. To ensure data quality, each rake was tested in a previously characterized flow to quantify measurement biases and sensitivity to yaw and pitch angles, or equivalently to swirl and radial flow angles in a propulsor flow.

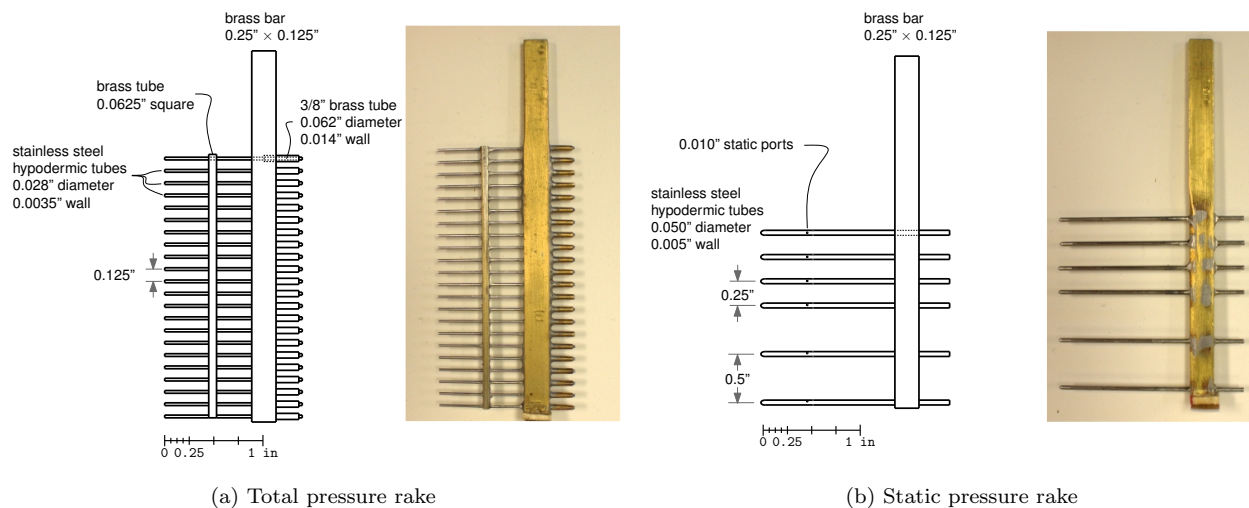


Figure 2: Pressure rakes used in wind tunnel experiments.

### B. Total Rake

#### 1. Construction

The total rake is shown in Figure 2a. The 22 pitot tubes are cut from 0.028” diameter, 0.0035” wall stainless steel hypodermic tubing stock, and are mounted in a 0.25”×0.125” brass bar. Each hypodermic tube is sheathed with a 0.0625” diameter brass tube at the back end for firm attachment of the pneumatic tubing. Each brass tube is 0.375” long but is embedded 0.125” into the brass bar, and hence protrudes 0.25” from the bar. All the hypodermic tubes pass through a 0.0625” square tube which provides additional support and also serves as an alignment jig during assembly, described below.

All these rake components can be made using basic machine tools. The hypodermic tubes are rapidly cut to the same length on a lathe. The tubing stock is cantilevered an exact amount from the lathe collet by butting it against a stop mounted in the tailstock. The tubing is scored with a pointed toolbit near the collet, and then snapped off. The end of the stock remaining in the lathe collet is then deburred and optionally chamfered inside, and the process is repeated for the next tube. The same process is used to cut and deburr the small brass tubes. The brass bar and square tube are drilled precisely on a milling machine. All the drilled holes are made oversize by about 0.002” to foster solder flow during assembly.

To prepare for soldering, oxidation is removed from all the rake components using very fine sandpaper or emery cloth, followed by degreasing with contact cleaner. Before assembly, it has been found beneficial

to pre-tin all the stainless steel tubes with soft solder and acid flux, using a soldering iron. Excess molten solder is wiped off to enable assembly of the rake. This pre-tinning promotes solder wicking in the final soldering step.

The assembly of the rake is eased by the fact that it is largely self-jigging. For alignment, it is only necessary to press the pitot tube ends against a flat surface and the their tips against a straightedge. Then the acid flux is applied to all the metal joints with a pipette, followed by heating with the soldering iron and application of the solder. The soldering iron must have a large thermal mass so that it is not quenched by the rake brass bar. Cleaning all oxidation from the solid-core solder helps quick wicking into all the joints.

The use of soft solder and soldering iron is very much easier than the alternative of using silver solder with a torch. The relatively low temperature of the iron also has the advantage that it does not soften the hypodermic tubing metal. The soft solder joints have proven to be more than strong enough in use.

## 2. Measurement quality

The pitot tubes of an ideal total pressure rake report the same total pressure for any flow angle. As shown in Figure 3, the present total rake has less than  $0.01 C_{p_o}$  deviation for flow angles within about  $\pm 15^\circ$ , if the transducer uncertainty is taken into account. With about 1 m of tubing between the rake and pressure transducer, the settling time is less than 1/2 second.

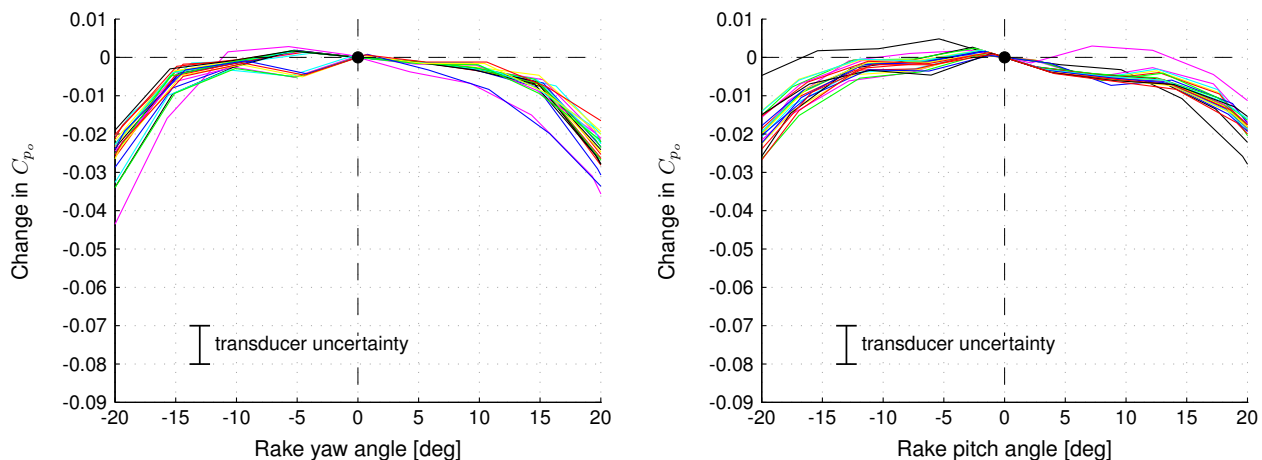


Figure 3: Total pressure measurement deviation due to change in total rake orientation.

## C. Static Rake

### 1. Construction

The static rake consists of six individual static tubes arranged as shown in Figure 2b. Because commercial static tubes of the appropriate size were not available, the tubes were constructed in-house with roughly 1 hour of labor each and negligible material costs.

The tubes are cut with the lathe technique from 0.050" diameter, 0.005" wall stainless steel hypodermic tubing stock. Four 0.010" static ports are drilled around the tube circumference, 0.5" (10 diameters) from the tip. The drilling is performed on a milling machine using a size 00000 center drill bit with a 0.010" pilot diameter. A knob attached to the tube enables precise rotation by  $90^\circ$  for the drilling of each port.

The port holes are deburred by polishing with a fine oilstone until no burrs are visible under 10x magnification. The tip of the tube is sealed with a small brass-rod plug and soft solder with acid flux. It is then beveled on the lathe, and rounded with a fine file on the lathe by hand. Testing of 15 tubes showed that each one measured  $C_p = -0.01 \pm 0.002$  in the uniform flow of a small open-jet wind tunnel, so that static tubes built with this technique are highly consistent.

To form the static rake, 6 static tubes are mounted in the same  $0.25" \times 0.125"$  size brass bar used for the total rake, except here the leading edge of the bar is given an elliptical shape (by hand filing) to minimize its upstream static-pressure disturbance. The rake is assembled using soft solder and acid flux, with a large soldering iron.

## 2. Measurement quality

Although the individual static tubes consistently measured  $C_p = -0.01$  in uniform flow, when mounted on the rake this changed to between  $C_p = -0.02$  and  $C_p = -0.05$  depending on the tube location. The difference is attributed to the mutual blockage influence of all the static tubes in proximity. These nonzero  $C_p$  values are treated as corrections which are removed to obtain the final measured data.

Static tubes typically are less tolerant of flow misalignment than pitot tubes, and Figure 4 shows the change in  $C_p$  due to rake yaw and pitch misalignment. The  $C_p$  errors are less than 0.01 for angles within  $\pm 5^\circ$ . With about 1 m of tubing between the rake and pressure transducer, the settling time is less than 1 second.

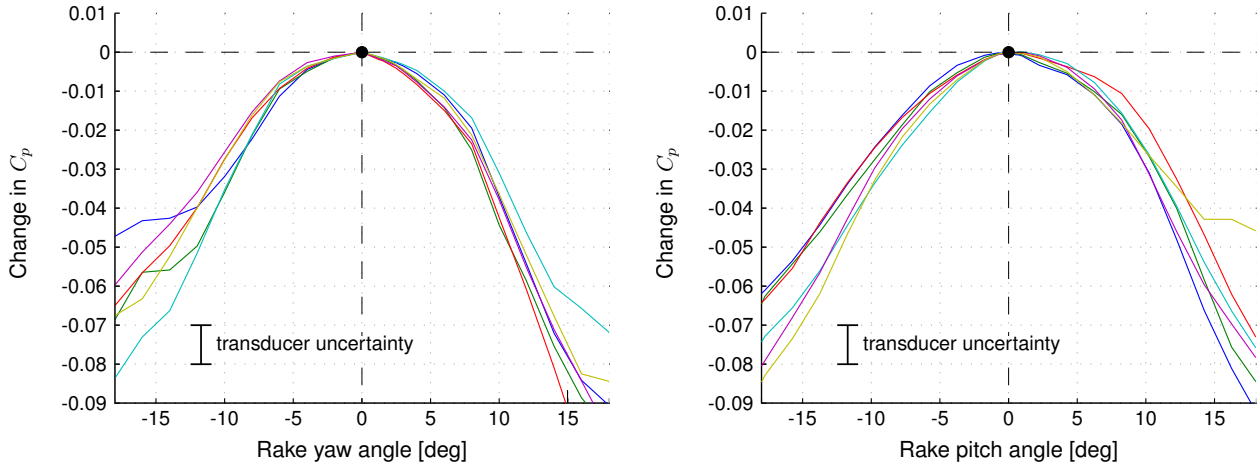


Figure 4: Static pressure measurement deviation due to change in static rake orientation.

## III. Rotating Rake System

### A. Mechanisms and Instrumentation

The rake support system, shown in Figures 5 and 6, consists of an aluminum vertical tower, an aluminum horizontal arm, and a steel forward arm reaching to the rake/motor beam which holds the rake and driving motor. The vertical tower is attached to the model support, so that the entire rake system is fixed relative to the model for any model angle of attack or sideslip angle.

The rake shaft is 1/4" precision-ground steel, and rotates in a reamed hole made directly in the bottom of the rake/motor mounting beam, made from 3/8"  $\times$  3/4" steel stock. To reduce the beam's flow disturbance it is thinned everywhere except at the bearing hole to a 1/8"  $\times$  3/4" cross-section with a rounded leading edge. The rake rotation is actuated by a NEMA 17-size hybrid stepper motor, which has a substantial 1.65" square cross section. To minimize its aerodynamic disturbance the motor was given a 3D-printed nose fairing, and was positioned at the top of the rake/motor beam roughly 7.5" above the rake shaft. The motor and the rake rotation shaft are connected by a 0.25" wide timing belt riding on two 0.625" diameter pulleys. The belt is tensioned by adjusting the motor-mount position on the beam.

The stepper motor is controlled by a QJ-215 Microstep Driver. The smallest rake angular position resolution is the same as the motor's resolution of 200 steps/rev, or  $1.8^\circ$ . During the experiments double steps of  $3.6^\circ$  were commanded for the total rake, and quadruple steps of  $7.2^\circ$  were commanded for the static rake. The rake positioning was performed automatically by the experiment control software, at a rate appropriate for the settling time of the rake.

The rake pressures were measured with an electronic differential pressure scanner system made by Measurement Specialties (model ESP-32HD and DTC Intium). The pressure scanner was mounted on the horizontal arm of the support structure, and connected to the rake by 0.040" pneumatic vinyl tubing roughly 1 meter in length. It is important to minimize the connection tubing length to give fast settling times.

The rake setups for the propulsor inlet and outlet shared all the mechanisms and instrumentation described above, and differed mainly in the length of the forward arm and in the rake attachment to the rotation shaft. For the inlet measurements, the rake was mounted directly to the shaft as shown in Figure 6

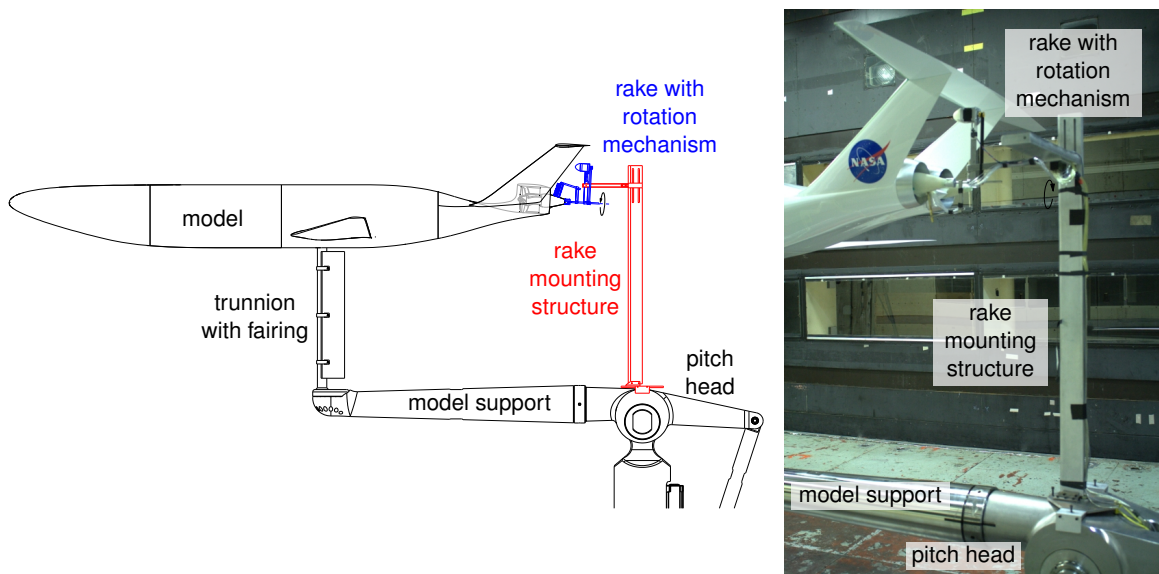


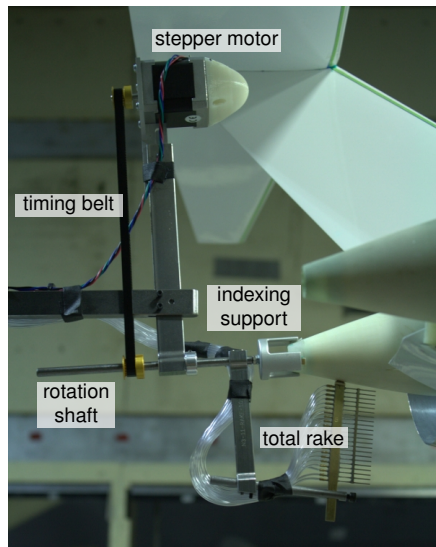
Figure 5: Rotating rake system mounted behind the model with an overview of rake positioning adjustments.

on the left. For the outlet measurements, the rake was mounted on the shaft through an additional radial arm and connecting rod, as shown in Figure 6 on the right. The connections between these components were adjustable, and were clamped with set screws.

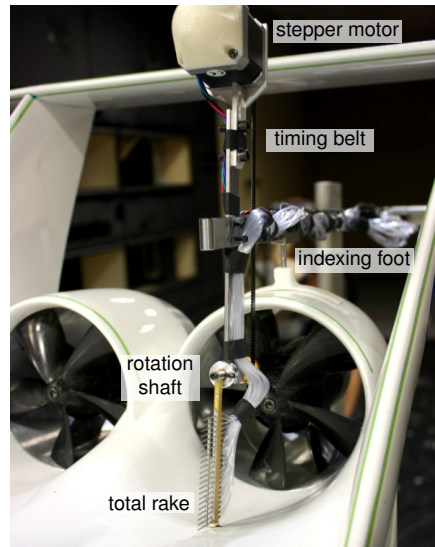
## B. Rake Positioning and Indexing

Coarse and fine position adjustments of the rakes could be made as indicated in Figure 5. Note that the steel forward arm is mounted by angle brackets whose angles align the forward arm with the propulsor axis, which is toed out  $3^\circ$  relative to the airframe centerline. Fine position adjustments were made to position the rake properly relative to the model. The forward arm was sized to have a sufficient amount of compliance so that the precise rake position was indexed by having the mechanism contact the model near the rake.

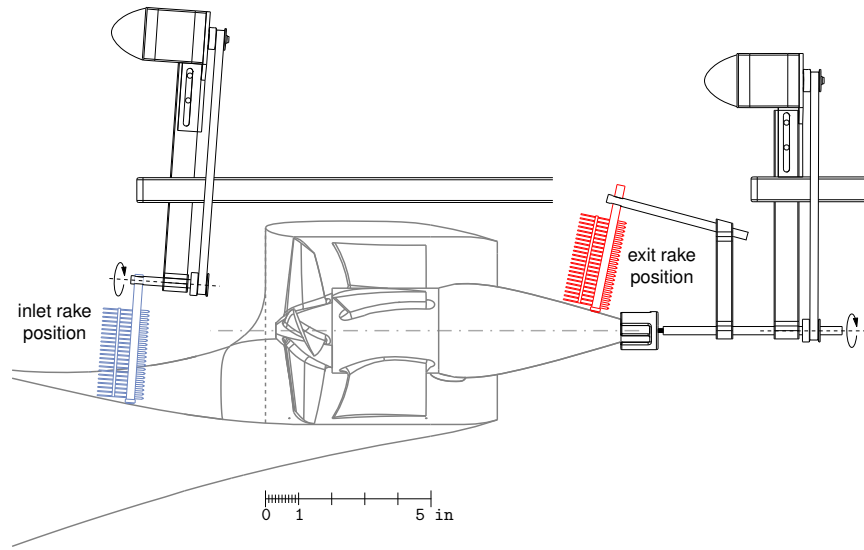
In the propulsor inlet rake setup, the contact was a plastic saddle which was mounted on the bottom of the forward arm, and which rested on top of the propulsor nacelle. The forward arm was thus indexed to the propulsor. The slight remaining compliance between the forward arm index point and the rake was controlled by letting the bottom end of the rake contact the model surface. A small teflon foot mounted on



(a) Total rake at exit measurement plane



(b) Total rake at inlet measurement plane



(c) Total rake at exit plane

Figure 6: Rake positioning for inlet and exit surveys for the integrated configuration.

rake allowed this contact point to slide freely on the model surface as the rake rotated.

In the propulsor exit rake setup, the rake rotation shaft had a “fork” which contacted the rear cone of the propulsor’s exhaust plug to precisely index the rake relative to the propulsor. This rake was again allowed to contact the exhaust plug through a teflon foot.

Figure 6 shows photos [(a) and (b)] and a schematic (c) of the rake positions at the inlet and exit survey locations. The inlet survey plane was located roughly  $0.90 D_{fan}$  upstream of the nacelle leading edge. This distance was chosen because it was the closest to the inlet plane while being able to safely route pressure tubing without risk of contact with the fan. The exit survey plane was located roughly  $0.35 D_{fan}$  downstream of the propulsor trailing edge. This was the closest distance to the propulsor trailing edge while still being able to capture the full jet stream. Any closer distance would cause the rake to interfere with the extended tail that comes out between the nacelles, and a portion of the jet would not be captured. To document the survey plane locations, detailed measurements were made relative to the nacelle inlet and exit plane for the inlet and exit surveys respectively. The exit rake tubes were closely aligned with the local exhaust flow

direction by pitching the rake relative to the rotation shaft.

### C. Rake Traverse Grids

The total pressure surveys at the propulsor exit consist of 100 angle positions over  $360^\circ$ . With the 22 rake tubes, a total of 2200 total-pressure grid points were measured per survey. The exit static pressure surveys have 50 angle positions, with the six static rake tubes which gives a total of 300 static-pressure grid points. At the propulsor inlet the topmost 4 angle positions were omitted due to the rake tubing interference with the motor/rake beam. The 96 positions then gave grids of 2112 points for the total rake and 288 points for the static rake. Figure 7 shows the rake survey grids at the exit and inlet.

One total pressure survey takes about fifteen minutes to complete and one static pressure survey takes about seven minutes to complete. Obtaining the same data with a single five-hole probe would require about 5.5 hours. And since such a single probe cannot be indexed locally to the model, the inevitable model and rake support deflections under airloads must be accounted for in some manner. The rapid data acquisition and spatial precision of the present rotating rake system are two of its major advantages.

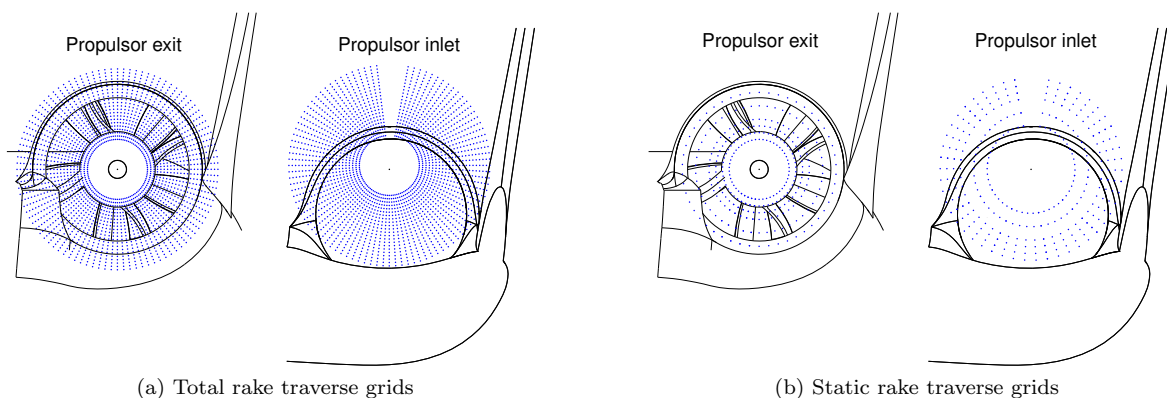


Figure 7: Rake traverse grids of survey points.

## IV. Pressure Field Measurements

Figure 8 shows example measured total and static pressure fields from the rotating rakes for the D8 experimental model, at the propulsor inlet and exit plane locations shown in Figure 6. These measurements were performed to determine the nature of the boundary layer fluid being ingested into the propulsor, and to determine the distribution of total pressure over the exit flow.

Subfigure 8a shows the inlet-plane total pressure distribution at a relatively high angle of attack condition,  $\alpha = 6^\circ$ ,  $C_L \simeq 1.05$ , where the boundary layer fluid shows the beginning of a roll-up into a stream-wise vortex. Subfigure 8c shows the distribution at the cruise condition,  $\alpha = 2^\circ$ ,  $C_L \simeq 0.65$ . Here the boundary layer fluid has a more benign “stratified” distribution which helps in minimizing adverse impacts on the fan performance. Subfigures 8b and 8d confirm the generally positive static pressure coefficient at the inlet plane which was a design objective in the shape design of the D8 fuselage.

Subfigure 8e at the exit plane shows the jet total pressure distribution. The wakes of the four stator vanes are visible, with the vane at the 4 o’clock position showing a small separation region. The exit total pressure rake extends well beyond the jet, and thus captures the wakes from the thin nacelle boundary layer, a portion of the vertical fin boundary layer, and the much thicker bottom-fuselage boundary layer.

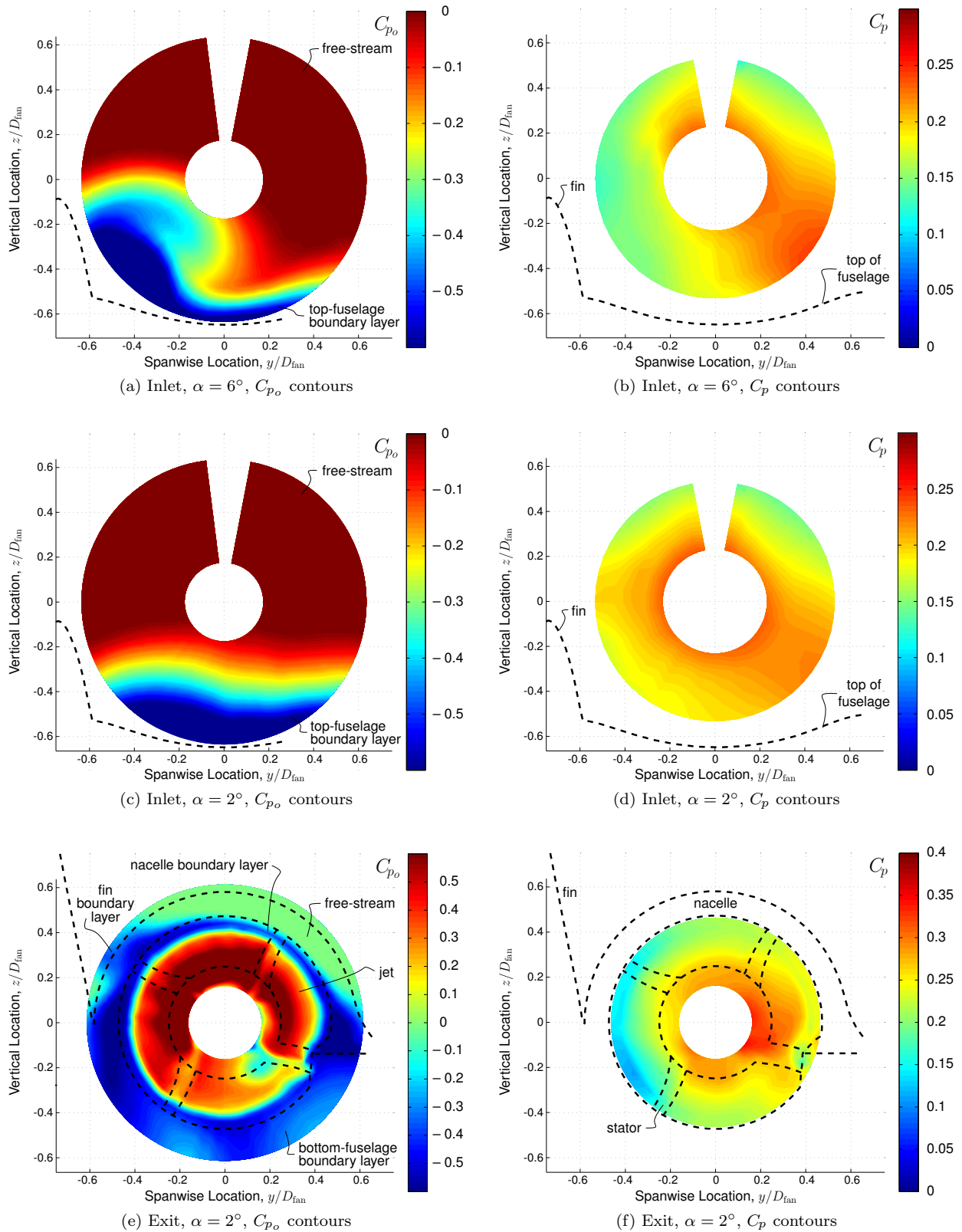


Figure 8: Total pressure and static pressure distributions measured with the rotating rakes, at the left-propulsor inlet in subfigures a) . . . d), and at the left-propulsor exit in subfigures e), f). The dashed curves indicate the various model surfaces and stator vanes. Tunnel conditions are  $Re = 5.5 \times 10^5$ ,  $\alpha = 6^\circ, 2^\circ$ ,  $\beta = 0^\circ$ . Fan speed ratio is  $U_{tip}/V_\infty = 1.924$ .

## V. Pressure Field Processing and Integration

The total and static rake pressure data is recorded as the standard total and static pressure coefficients, which largely compensates for minor drift of the tunnel flow conditions over the duration of the rake survey.

$$C_{p_o} = \frac{p_o - p_{o\infty}}{q_\infty} \quad (1)$$

$$C_p = \frac{p - p_\infty}{q_\infty} \quad (2)$$

Subsequent calculations involve both of these coefficients. Since the static pressure survey grids are coarser, the static pressure coefficient data is transferred to the total pressure grid point locations by linear interpolation in the radial and circumferential directions. This then allows calculation of the velocity ratio  $V/V_\infty$  on the total-pressure survey grid.

$$\frac{V}{V_\infty} = \sqrt{C_{p_o} - C_p + 1} \quad (3)$$

Quantities computed from the rake survey data include the non-dimensionalized jet total pressure flux  $\tilde{C}_{P_K}$  and the non-dimensionalized propulsor jet mass flow.

$$\tilde{C}_{P_K} = \iint_{A_{\text{jet}}} -C_{p_o} \frac{\vec{V}}{V_\infty} \cdot \hat{n} \frac{dA}{S_{\text{ref}}} \quad (4)$$

$$\frac{\dot{m}_{\text{jet}}}{\rho V_\infty A_{\text{fan}}} = \iint_{A_{\text{jet}}} -\frac{\vec{V}}{V_\infty} \cdot \hat{n} \frac{dA}{A_{\text{fan}}} \quad (5)$$

Evaluation of the normal velocity component in the integrals above requires knowing the velocity magnitude as well as its direction, whereas the rake data provides only the magnitude via equation (3). In the present study the flow angles were extracted from a FLUENT computation of the isolated propulsor. Since the jet flow direction is within a few degrees of being normal to the integration plane, sketched in Figure 9, we have  $\vec{V} \cdot \hat{n} \simeq V$ , and hence the flow angles from the FLUENT calculation have a small effect on the integrated parameters. The sensitivity of the computed results to the flow angles will be examined in the next section.

A more significant effect comes from the location of the outer boundary of the area of integration, shown in Figure 9. This is defined as the radial location where

$$C_{p_o} = C_{p_{\text{st}}} \quad (6)$$

is reached. Here  $C_{p_{\text{st}}}$  is some chosen threshold total pressure coefficient value which defines the integrated-streamtube boundary. Ideally this is slightly positive so that streamlines which do not pass through the propulsor are excluded from the integration (aside from those entrained into the jet in the short distance between the nozzle plane and the rake measurement plane). The sensitivity of the integrated parameters to the chosen  $C_{p_{\text{st}}}$  value will be examined in the next section.

The area integrals (4) and (5) are evaluated using 2D trapezoidal integration on the fine total pressure grid, using the threshold value  $C_{p_{\text{st}}} = 0.01$ . The results are shown in Figure 10 for three different propulsor power settings. The vertical axis parameter  $C_X$  is the net stream-wise force coefficient,

$$C_X = \frac{F_X}{q_\infty S_{\text{ref}}} \quad (7)$$

$$= \frac{\text{drag} - \text{thrust}}{q_\infty S_{\text{ref}}} \quad (8)$$

where the second definition (8) would be used for a conventional aircraft with isolated propulsors. Because the propulsion system is integrated into the D8 airframe, there is no unique way to separately define drag and thrust; only the net stream-wise force  $F_X$  is uniquely defined and is measured with the model's force balance.

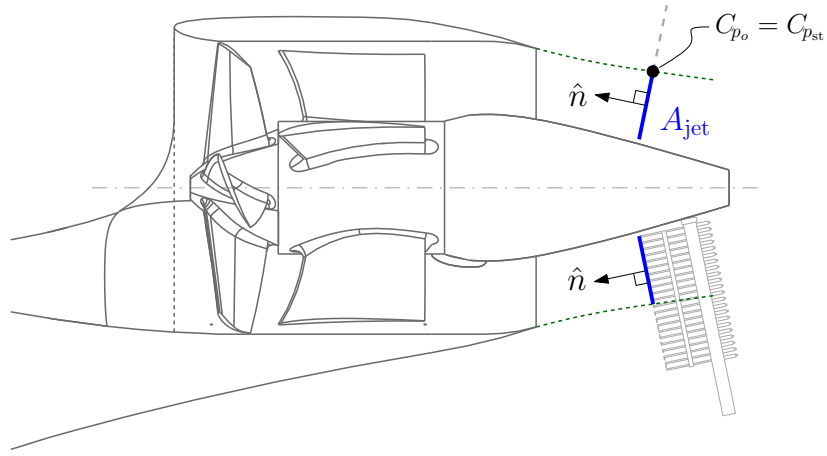


Figure 9: Schematic of the integration region for the exit traverses.

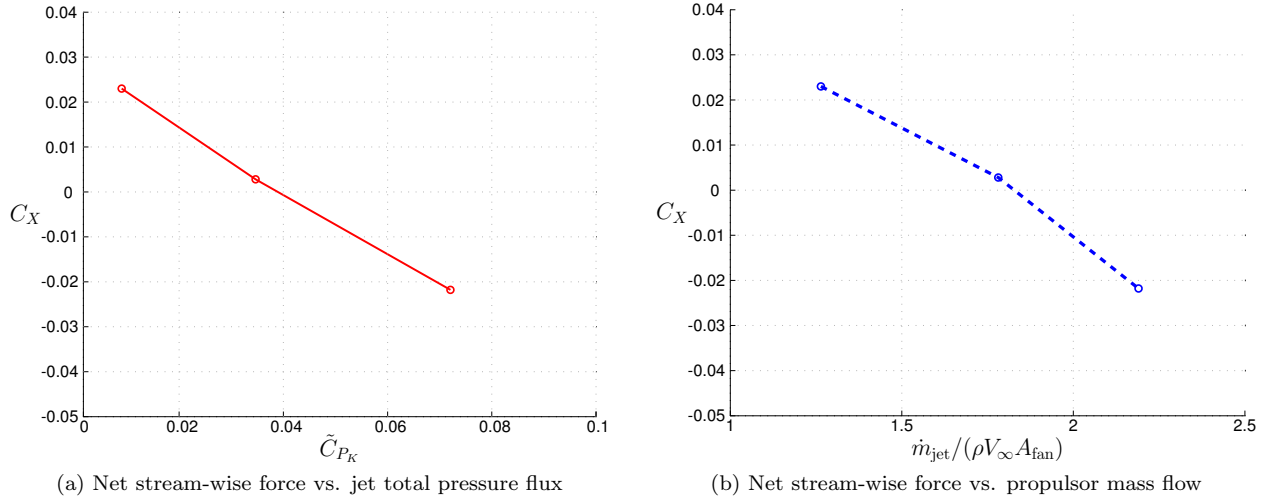


Figure 10: D8 model net stream-wise force coefficient measured with force balance, versus propulsor parameters computed from jet survey measurements, for three propulsor power settings. All three cases have  $Re = 5.5 \times 10^5$ ,  $\alpha = 2^\circ$ ,  $\beta = 0^\circ$ . The integration threshold value  $C_{p_{st}} = 0.01$  is used here.

## VI. Sensitivities of Computed Parameters

### A. Sensitivity Assessment

Calculation of the integrated parameters defined by equations (4) and (5) from the rake survey data involved two main assumptions. First, the velocity direction (but not magnitude) was assumed to be correctly given by the FLUENT computations. Second, the area of the integration was assumed to be appropriately defined by the chosen value of the threshold total pressure coefficient  $C_{p_{st}}$ . This section quantifies the sensitivity of the integrated parameters to the flow angles and the  $C_{p_{st}}$  value and the sensitivity to uncertainties in the pressure-measurement instrumentation. The sensitivity studies are performed at conditions of  $Re = 5.5 \times 10^5$ ,  $\alpha = 2^\circ$ ,  $\beta = 0^\circ$ , and  $U_{tip}/V_\infty = 2.64$ .

## B. Sensitivity to Flow Angles

The direction of the velocity vector in the integrals in equations (4) and (5) is defined here by the radial and swirl flow angles  $\theta_{\text{rad}}$  and  $\theta_{\text{swl}}$ . Their baseline distributions over the integration area were extracted from the FLUENT calculation. The entire distribution of each angle was systematically shifted by a perturbation over the range  $\Delta\theta = \pm 10^\circ$ , and the integral parameters were recomputed for each perturbation.

The variation in the integral parameters resulting from the radial and swirl angle perturbations are shown in Figure 11. All the curves closely correspond to a cosine function, as can be expected from the  $\vec{V} \cdot \hat{n}$  dot product in the flux integrals (4) and (5). The peak of the cosine is where the average velocity vector is normal to the integration area and hence the dot product is at a maximum. An important observation is that the integral parameters are within 1% of their baseline values over a flow angle perturbation range of  $\Delta\theta = -8^\circ \dots +5^\circ$ . This small sensitivity justifies the use of flow angles from the CFD calculations to augment the rake survey measurements.

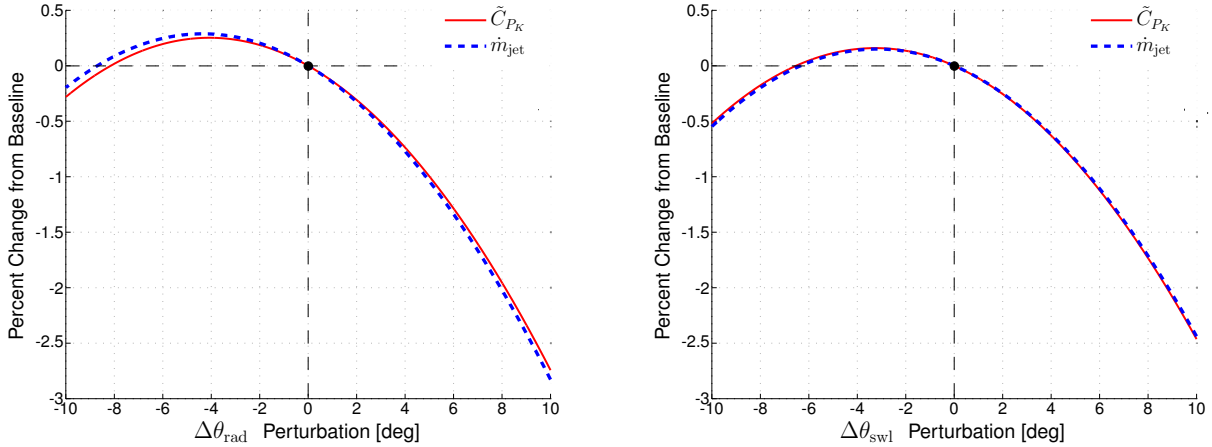


Figure 11: Integrated parameter sensitivities to changes in assumed radial and swirl flow angles.

## C. Sensitivity to Threshold Pressure Coefficient

To investigate the effect of the streamtube-boundary threshold total pressure coefficient  $C_{p_{\text{st}}}$  on the integral parameters,  $C_{p_{\text{st}}}$  was systematically varied from -1.0 to 3.0, with the integral parameters recomputed for each value. Figure 12 shows the resulting integral parameter perturbations versus  $C_{p_{\text{st}}}$ .

The  $\tilde{C}_{P_K}$  sensitivity curve has several distinct features. Theoretically  $\tilde{C}_{P_K}$  is at a maximum at  $C_{p_{\text{st}}} = 0$ , since a negative  $C_{p_{\text{st}}}$  will result in negative  $C_{p_o}$  contributions to the integral, decreasing its value, while a positive  $C_{p_{\text{st}}}$  will decrease the area of integration, again reducing the overall integral value. The unexpected change of +0.05% in  $\tilde{C}_{P_K}$  for slightly positive  $C_{p_{\text{st}}}$  is attributed to slightly positive values of measured total pressure coefficient in the free-stream regions due to pressure transducer measurement uncertainty.

The integrated mass flow monotonically increases as  $C_{p_{\text{st}}}$  is decreased. Especially notable is the sharp increase in  $\dot{m}_{\text{jet}}$  as  $C_{p_{\text{st}}}$  drops below  $-0.015$ , due to an increase in the integration area which now includes the free-stream portions of the survey grid. This justifies the small positive  $C_{p_{\text{st}}} = +0.01$  choice.

## D. Effect of Instrumentation Errors

Instrumentation errors can also affect the pressure rake data. The main source of error for the static rake is susceptibility to flow angularity. This can be estimated using the measured static rake flow-angle error shown in Figure 4, together with the flow angles obtained from the CFD calculation, which indicates that the exit traverse static rake sees radial flow angle deviations of  $\Delta\theta_{\text{rad}} = -3^\circ \dots 7^\circ$  and swirl flow angle deviations of  $\Delta\theta_{\text{swl}} = 0^\circ \dots 5^\circ$ . From Figure 4 this corresponds to an error in the measured static pressure coefficient of at most  $\Delta C_p = -0.014$ . The total rakes are less sensitive to flow angle deviation, and their maximum error is only  $\Delta C_{p_o} = -0.005$ .

To evaluate the sensitivity of the integrated parameters to these rake measurements errors, the entire measured  $C_p$  and  $C_{p_o}$  fields are systematically biased by the range of perturbations  $\Delta C_p = -0.1 \dots 0.1$ , and

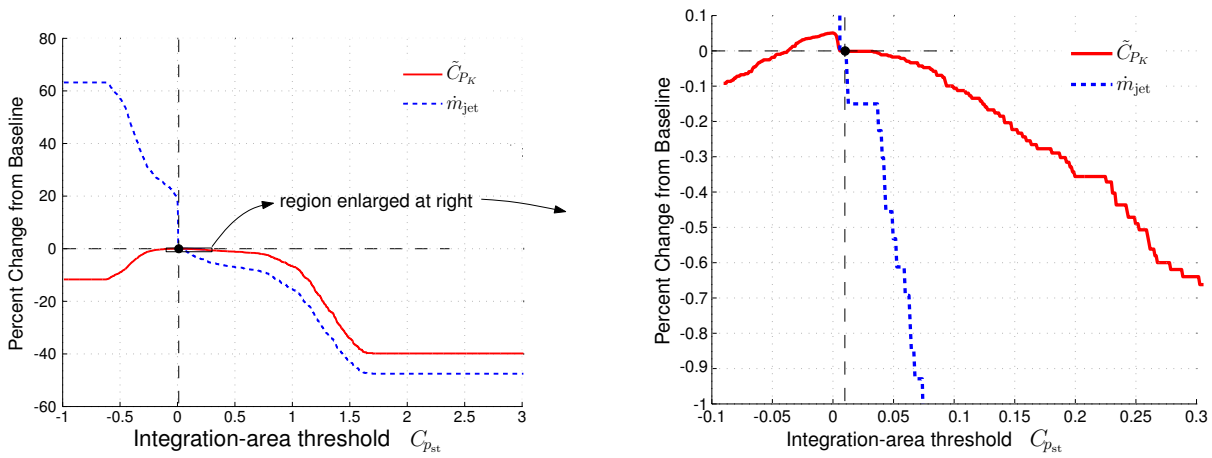


Figure 12: Sensitivity to choice of integration-area threshold total pressure coefficient  $C_{p_{st}}$ . Baseline values correspond to  $C_{p_{st}} = 0.01$ .

$\Delta C_{p_o} = -0.01 \dots 0.01$ , and the  $\tilde{C}_{P_K}$  and  $\dot{m}_{jet}$  integrals are recomputed for each perturbation. The results are shown in Figure 13.

An increasing  $\Delta C_p$  perturbation results in monotonically decreasing  $\tilde{C}_{P_K}$  and  $\dot{m}_{jet}$ . This is to be expected since an increase in  $C_p$  directly decreases  $V/V_\infty$ , as seen from equation (3). The result is a decrease in the total pressure flux and mass flux in equations (4) and (5). An important conclusion is that the  $-0.014$  uncertainty in  $C_p$  due to flow angularity produces less than  $0.5\%$  change in the integrated parameters.

An increasing  $\Delta C_{p_o}$  perturbation produces monotonically increasing  $\tilde{C}_{P_K}$  and  $\dot{m}_{jet}$ , although the trends in the two parameters are different. The change in  $\tilde{C}_{P_K}$  is from three effects. The largest effect is from the explicit appearance of  $C_{p_o}$  in the  $\tilde{C}_{P_K}$  integrand in equation (4), noting that  $\vec{V} \cdot \hat{n}$  is negative. A weaker second effect is the influence of  $C_{p_o}$  on  $V/V_\infty$  via equation (3). The third effect, also weak, is the influence of  $C_{p_o}$  on the integration area via the fixed  $C_{p_{st}}$  threshold. The effect on  $\dot{m}_{jet}$  is solely due to the  $V/V_\infty$  contribution. The sharp increase at  $\Delta C_{p_o} = 0.004$  is due to a sudden increase in the integration area as the free-stream portions of the  $C_{p_o}$  field begin to approach the  $C_{p_{st}} = 0.01$  threshold. The sharp increase can be postponed by increasing  $C_{p_{st}}$  as needed. The  $\pm 0.005$  uncertainty in  $C_{p_o}$  due to the pressure transducer uncertainties implies a maximum  $0.5\%$  uncertainty in the integrated  $\tilde{C}_{P_K}$  value, and a maximum  $2\%$  uncertainty in the integrated mass flow.

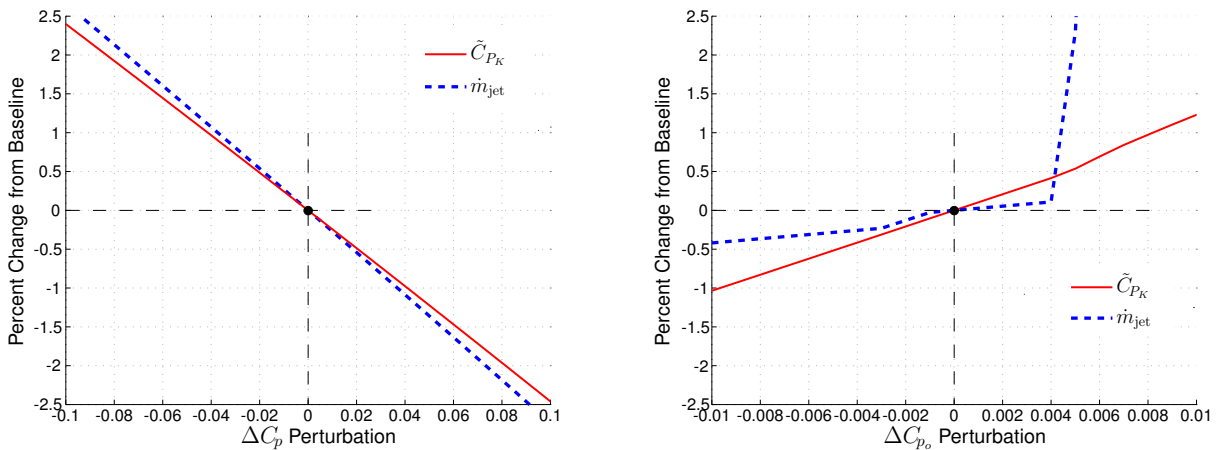


Figure 13: Sensitivity of integrated parameters to static (left) and total (right) pressure coefficient variations.

## VII. Summary and Conclusions

This paper illustrates the use of a rotating rake system for effective flow field measurements. Separate total and static pressure fields from the rake system can be merged to calculate other related local and integrated flow field quantities of interest.

The rotating rake used in the N+3 experiments provided rapid pressure measurements which allowed exploration of a wide range of operating conditions for a given tunnel time. The compactness of the rake system allowed measurements in planes immediately upstream and downstream of integrated propulsors. The total cost for the rake materials was less than \$100 for two rakes, and the commercially available items that drove the rotation, specifically the stepper motor, motor controller, timing belts and gears, cost under \$90. The rakes were constructed using only common machine tools.

The rotating rake system does have some limitations. One is the sensitivity to flow angularity. For  $C_{p_o}$  errors less than 0.01, the total rake could tolerate flow angles within  $\pm 15^\circ$ , while for  $C_p$  errors of less than 0.01 the more sensitive static rake could tolerate angles within  $\pm 8^\circ$ . Fortunately, the jet total pressure flux, the quantity of interest in the experiments, is not sensitive to errors in the measured static pressure field or flow angularity.

One improvement to the system that is specific to the N+3 application is to be able to measure at the actual propulsor inlet and exit planes. Due to the rake size and shape, full surveys at the propulsor trailing edge were impossible. This can be solved by making the rake shorter and contouring the rake to avoid obstructions. By making this change, the need to set a integration area threshold is avoided because the area of interest would be defined by the propulsor geometry. The upstream propulsor surveys can also be closer to the inlet with some re-routing of the pressure tubing. The relative speed and ease of the manufacture of the rakes described here makes it feasible to build custom rakes to match any special experimental geometry. It would also be possible to make pitot-static rakes which would avoid the need to survey the flow field twice with two different rakes.

## Acknowledgments

The work is supported by the NASA's Fundamental Aeronautics program, Fixed Wing project who provided funding for the project. The authors are only a part of a larger team and this work would not be possible without the help of the N+3 team. The authors would like to extend their gratitude to the members of the Aurora Flight Sciences N+3 team who supported the experimental effort, specifically Ben Smith who led the structural design of the rake system support. The authors would also like to acknowledge Dr. Neil Titchener and Alex Feldstein who conducted the total pressure rake measurement assessment.

## References

- <sup>1</sup>et al., E. G., "N+3 aircraft concept designs and trade studies, Final Report," *NASA CR 2010-216794*, 2010.
- <sup>2</sup>Drela, M., "Development of the D8 transport configuration," *29th AIAA Applied Aerodynamics Conference, Honolulu, HI, AIAA Paper 2011-3970, 27-30 June 2011*, 2011.
- <sup>3</sup>Drela, M., "Power balance in aerodynamic flows," *AIAA Journal*, Vol. 47, No. 7, 2009, pp. 1761–1771.

## References

- <sup>1</sup>Sutliff, Daniel L., "Rotating Rake Turbofan Duct Mode Measurement System", NASA/TM 2005-213828, Oct. 2005
- <sup>2</sup>Drela, M., "Development of the D8 transport configuration", 29<sup>th</sup> AIAA Applied Aerodynamics Conference, 27-30 June 2011, Honolulu, HI, AIAA Paper 2011-3970
- <sup>3</sup>Drela, M., "Power Balance in Aerodynamic Flows", 27<sup>th</sup> AIAA Applied Aerodynamics Conference, 22-25 June 2009, San Antonio, TX, AIAA Paper 2009-3762
- <sup>4</sup>Greitzer, E.M., et al., "N+3 Aircraft Concept Designs and Trade Studies, Final Report", NASA CR 2010-216794, Dec. 2010